

Structural Parameters of the Globular Cluster M 15

M. V. Petkova^{1,*}, G. P. Petrov¹, N. M. Kacharov² and P. L. Nedialkov¹

¹ Faculty of Physics, Department of Astronomy, Sofia University ‘St. Kliment Ohridski’, 5 J. Bourchier Blvd., Sofia 1164, Bulgaria; mpetkova@phys.uni-sofia.bg

² Leibniz Institute for Astrophysics (AIP), An der Sternwarte 16, 14482 Potsdam, Germany

Received 2025 November 22; accepted 2026 March 12

Abstract We present a detailed analysis of the structural parameters of the globular cluster M 15 using g- and i-band photometric data from Pan-STARRS1 DR2. The central coordinates (X_C , Y_C), ellipticity (ϵ), and position angle (PA) are derived via two independent methods: ellipse fitting of the two-dimensional stellar number isodensity distribution and Markov Chain Monte Carlo (MCMC) sampling. Our analysis of 38 stellar density intervals reveals a cluster center offset by only $4''.1 \pm 9''.6$ from the commonly accepted in the literature value, a good agreement on the order of our map resolution. We find a radial variation in the ellipticity, with a mean value of $\epsilon = 0.09 \pm 0.02$ for the inner region ($R \leq 4'.5$) and $\epsilon = 0.04 \pm 0.02$ for the outer region ($R > 4'.5$), where the errors correspond to 1σ . The MCMC analysis of 75 datasets yields a mean $\epsilon = 0.022 \pm 0.005$ for the entire cluster. The PA remains constant with increasing distance from the cluster center, $PA = 44^\circ.4 \pm 16^\circ.2$, and the MCMC method providing a consistent value of $PA = 46^\circ.6 \pm 7^\circ.1$. Our results are in agreement with some recent studies but challenge others, suggesting that a single ϵ value may be insufficient to fully characterize the overall oblateness of M 15 due to incompleteness and crowding effects in its core.

Key words: (Galaxy:) globular clusters: individual: M 15 — techniques: photometric — methods: data analysis

1 INTRODUCTION

Globular clusters (GCs) are gravitationally bound stellar systems, containing from tens of thousands to millions of stars. As some of the oldest objects in the Universe, they are of particular interest for understanding the early stages of galaxy formation and evolution. In the Milky Way, more than 200 GCs are known to exist (Garro et al. 2024), located predominantly in the halo, but also found in the bulge and the thick disk. A defining characteristic of GCs is their high stellar concentration, with densities reaching extreme levels toward their centers. While often idealized as spherical, it has been known since the early 20th century that many GCs exhibit deviations from this shape, appearing as oblate spheroids (for a historical overview, see Chen & Chen 2010). This deviation is commonly quantified by the apparent ellipticity, $\epsilon = (1 - b/a)$, where a and b are the projected major and minor axes, respectively. The Harris (1996, 2010 edition) catalog compiled comprehensive data for 157 GCs, providing ellipticity estimates for 100 of them. More recently, Cruz Reyes & Anderson (2024) listed the ellipticities for 163 Galactic GCs in their catalog.

*Corresponding Author

M 15 (NGC 7078) is one of the oldest known GCs in the Milky Way, with an estimated age of approximately 13 Gyr (Baumgardt et al. 2023) and a mass of $5.18 \times 10^5 M_{\odot}$ ¹. Historically, it is considered a prototypical core-collapsed cluster, characterized by a surface density profile that rises steeply into the center – a morphology standing in marked contrast to the flat central cores of standard King-model clusters (Gerssen et al. 2002). This central density cusp has long fueled the debate over whether M 15 harbors an intermediate-mass black hole (IMBH) or has undergone a gravothermal core collapse. Most recently, Huang et al. (2025) provided compelling kinematic evidence for an IMBH by identifying a hypervelocity star ejected from the cluster’s center, effectively resolving this long-standing dynamical puzzle. Beyond its dense core, the external dynamics of M 15 reveal a complex interaction with the Galactic potential. Utilizing high-precision astrometry from Gaia DR3, Chen et al. (2025) recently detected faint tidal streams associated with the cluster, allowing for a precise derivation of its mass loss rate. While this confirms that M 15 is subject to active tidal stripping, it is important to note that at the smaller radial scales probed in this work, these external tidal effects do not significantly influence the cluster’s intrinsic shape. However, the geometric structure of the cluster – specifically its ellipticity and position angle – remains a critical diagnostic for understanding its formation history and dynamical state. In the context of the classification proposed by Belokurov & Kravtsov (2024), M 15 is a probable candidate for an accreted system, potentially the stripped nucleus of a dwarf galaxy rather than an in-situ formed cluster. Such systems are expected to preserve internal rotation, which can result in a pronounced ellipticity in their inner regions (see, e.g., Botev et al. 2025). Therefore, precise measurements of geometric parameters may provide crucial constraints on these evolutionary scenarios: a detected inner ellipticity driven by rotation would support the stripped-nucleus hypothesis, while a spherical morphology would be more consistent with a non-rotating, pressure-supported system.

The main objective of this work is to derive the mean values of the structural parameters of M 15 – specifically its central coordinates (X_C, Y_C), ellipticity ϵ , and position angle (PA) – using photometric data from the Pan-STARRS1 (PS1) DR2² survey (Flewelling et al. 2020). These parameters are derived by applying ellipse fitting techniques and smoothing of two-dimensional (2D) density distribution at different angular scales.

This paper is organized as follows: Section 2 describes the data selection from the PS1 DR2 catalog and the filtering procedures applied. Section 3 details the two methods used to derive the structural parameters: ellipse fitting of the 2D number density distribution and discrete Markov Chain Monte Carlo (MCMC) sampling of the 2D number density distribution. The results are presented and compared with previous studies in Section 4. Finally, Section 5 provides a summary of the main conclusions of the work.

2 DATA SELECTION AND FILTERING

We retrieved the gi-band photometry data from the PS1 DR2 catalog centered on the coordinates of M 15: RA = $21^{\text{h}} 29^{\text{m}} 58^{\text{s}}.33$ and DEC = $+12^{\circ} 10' 01''.2$ (J2000), as listed in Goldsbury et al. (2010). The sources are required to have photometry in both the g- and i-bands, as this is necessary for subsequent analysis, such as filtering, constructing the color–magnitude diagram (CMD), etc. The availability of standard deviations for the photometry in both bands is also required, which will be used for the error assessment of our measurements.

To assess the impact of the field size on the obtained parameters, we downloaded the data for several angular scales. The selection of the largest field of view was guided by the cluster’s tidal radius, which is $27'.3$ (Harris 1996, 2010 edition). Consequently, we chose a $60' \times 60'$ to ensure the entire cluster was encompassed. Subsequently, we also extracted smaller fields of $50' \times 50'$, $40' \times 40'$, $30' \times 30'$, and $20' \times 20'$. The rationale for using these smaller fields relates to the cluster’s structure. M 15 is noted in the Harris catalog as a core-collapsed cluster, characterized by a much smaller core and effective radii, relative to its tidal radius. Since the vast majority of member stars are concentrated in this central

¹ <https://people.smp.uq.edu.au/HolgerBaumgardt/globular/>

² <https://outerspace.stsci.edu/display/PANSTARRS>

region, we assumed that the derived structural parameters should not differ significantly between the various field sizes.

At first, we applied a series of filtering steps to the data for each field size. We used quality flags (q) to distinguish between point-like and extended sources within the given g - or i -bands. To isolate stellar sources (point-like), a criterion of $q < 16777216$ was applied. This filtering was necessary to verify the extent to which the presence of objects (e.g., blended stars, background galaxies) flagged as "Extended in this band" ($q = 16777216$) in PS1 DR2 catalog (Flewelling et al. 2020) affects the estimated structural parameters.

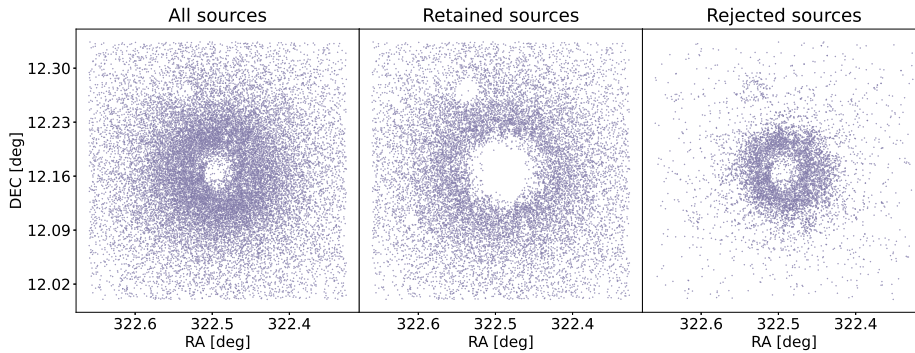


Fig. 1: Two-dimensional spatial distribution of the photometrically filtered stars of the GC M 15 in a $20' \times 20'$ field. The first panel from left to right shows the 2D distribution of the unfiltered sources, the second shows their distribution after filtering, and the third panel displays the 2D distribution of the rejected sources, which in this case satisfy the condition for the removal of extended objects in the g - or i -band (f4). As expected, these objects are predominantly located in the cluster's center and around the brightest stars.

We selected four types of filtration. The first is the removal of extended objects in the g -band (filtration f1). This left point-like objects in the g -band, while in the i -band, they can be either point-like or extended. We performed an analogous process for the i -band (filtration f2), which left point-like or extended sources in the g -band. The third filtration (f3) removed only the sources that are extended in both the g - and i -bands. In this case, sources that are point-like and those that are extended in only one of the two bands remained. The final case (f4) is the most precise filtration, that left only point-like sources in both g - and i -bands. An example of the filtration for a cluster in a $20' \times 20'$ field is shown in Figure 1, and the CMDs for each filtration type are illustrated in Figure 2.

Following the filtering process, we transformed the equatorial coordinates (RA, DEC) of the sources to tangential coordinates (X , Y), using the M 15 center coordinates given by Goldsbury et al. (2010).

Finally, based on the methodology of Lee & Carney (1999), we applied a contamination subtraction for the PS1 DR2 photometric data. For each field size, we selected two corresponding background fields. These are located 5° from the cluster's center, but at the same Galactic latitude to ensure uniform background density. These areas have been examined and are devoid of any large, bright objects. They are intended to be used for the removal of background contamination from the GC, provided that the object density within them corresponds to the background object density surrounding the GC. Comparing the CMDs of M 15 and the background field, upon matching with a field star within 3σ of g and $g-i$, we excluded background objects from the M 15 CMD.

Once each sample has been filtered and the background objects removed, the cluster's structural parameters can be derived.

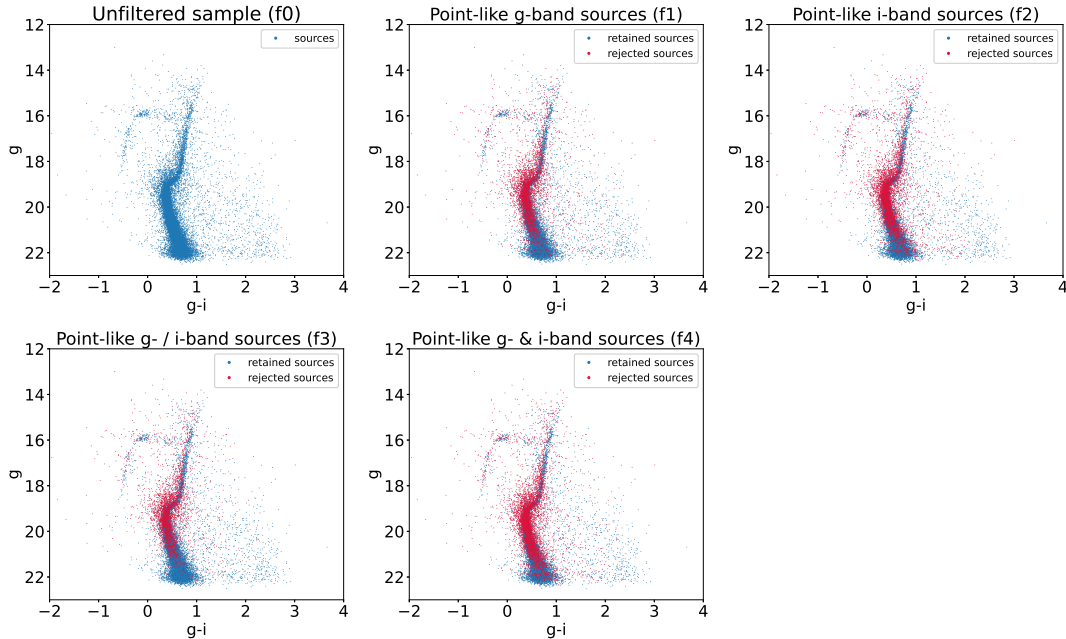


Fig. 2: CMDs of point-like sources (quality flag $< 2^{24} = 16777216$) in g- and i-bands within the $20' \times 20'$ field of M 15. The top-left diagram shows the unfiltered sample with all sources plotted in blue. Each subsequent diagram presents one filtering type: retained objects are marked in blue and rejected ones with red. As expected, f4 excludes the largest fraction of sources.

3 METHODS

3.1 Structural parameters derived from ellipse fitting of the 2D number density distribution

Here we analyze the unfiltered $40' \times 40'$ field of view centered on M 15, where the background contamination is accounted for, but the extended objects are not removed. We binned the data to generate the stellar number density, defined as the count of stars per pixel ($*/\text{px}$). We prefer stellar number density over the cluster's surface brightness, as it is less sensitive to individual bright stars or projected background contamination. Initially, the stellar density map was constructed using square pixels of $24'' \times 24''$ and $12'' \times 12''$, yielding arrays of 100×100 and 200×200 pixels, respectively. These pixel sizes were chosen as an optimal compromise. They are large enough to ensure sufficient star statistics per bin in the outskirts, yet small enough to resolve the structural changes in the inner regions without washing out the ellipticity signal.

After pixelizing the image, density thresholds can be applied directly to filter for a specific range of values, which is then used to derive the ellipse parameters. Alternatively, the map can be smoothed beforehand to reduce noise. Both approaches were tested for comparison. In the first case (unsmoothed), the density values are discrete, as they correspond to the integer number of stars in each pixel. In the second case, however, smoothing the cluster map resulted in continuous density values, which permitted a more refined selection of the density intervals.

We performed the smoothing using a 2D boxcar averaging method. This was implemented with a 3×3 or 5×5 kernel where each element has a weight of 1, while all elements outside this matrix have a weight of 0. A thorough validation of this smoothing procedure using mock density maps is presented in Appendix B, confirming that it introduces no systematic errors to the derived structural parameters.

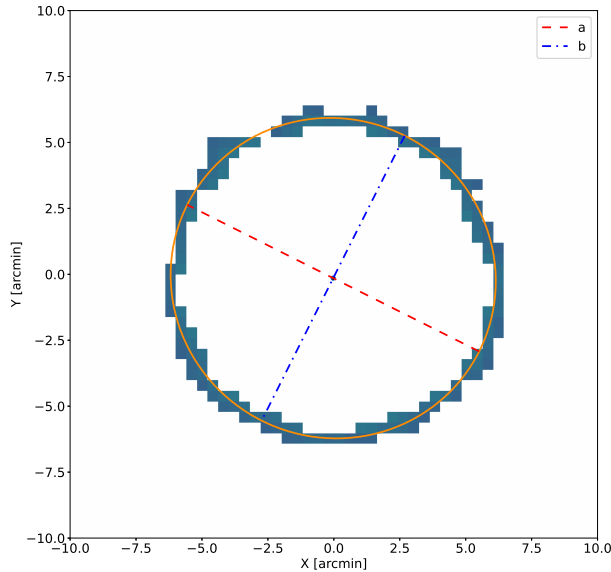


Fig. 3: Ellipse fitting over the $7\text{--}9$ */px density interval for the 100×100 array smoothed with a 5×5 boxcar. The major and minor axes are indicated by a red dashed line and a blue dash-dotted line, respectively. The fitted ellipse is drawn in orange and the isodensities are marked with blue pixels.

Following the smoothing procedure, we selected specific density intervals for analysis. These intervals were chosen to avoid regions very close to the cluster’s center, where data incompleteness can lead to spurious results. Similarly, we excluded the outermost parts of the cluster, as the data there is noisier and the densities are lower.

For each selected interval, we fitted an ellipse using the `EllipseModel` from the `scikit-image` Python package (van der Walt et al. 2014), which implements a least-squares algorithm. This fit yields the cluster’s structural parameters: the semi-major a and semi-minor b axes, the center coordinates (X_C, Y_C) , the position angle PA, and the ellipticity ϵ . An example of an ellipse fit for the $7\text{--}9$ */px density interval, applied to a 100×100 array smoothed with a 5×5 boxcar kernel, is shown in Figure 3.

We performed error estimation using the Bootstrap method (Efron 1979). This technique involves repeatedly generating new datasets by resampling the coordinates of the pixels within a given density interval. Crucially, this is done with replacement, meaning a single pixel’s coordinates can be selected multiple times in a new sample. This process is repeated 10 000 times, creating 10 000 bootstrapped datasets. An ellipse is then fitted to each of these, yielding a distribution of values for each parameter. We adopted the standard deviation of this distribution as the 1σ error for that parameter.

The results from the ellipse fitting for all considered 38 density intervals in the $40'\times 40'$ field are presented in Table A.1 and are shown graphically in Figure 4. Due to the contribution of extended objects (see Figure 1) the highest stellar density is observed between $1'$ and $3'$ from the cluster center. Although a torus-like structure appears when $24''$ binning is combined with 5×5 boxcar smoothing, the densities within $3'$ remain patchier in all other cases. Consequently, we adopt an inner fitting radius of $\sim 3'$ for all samples in order to avoid the influence of extended sources.

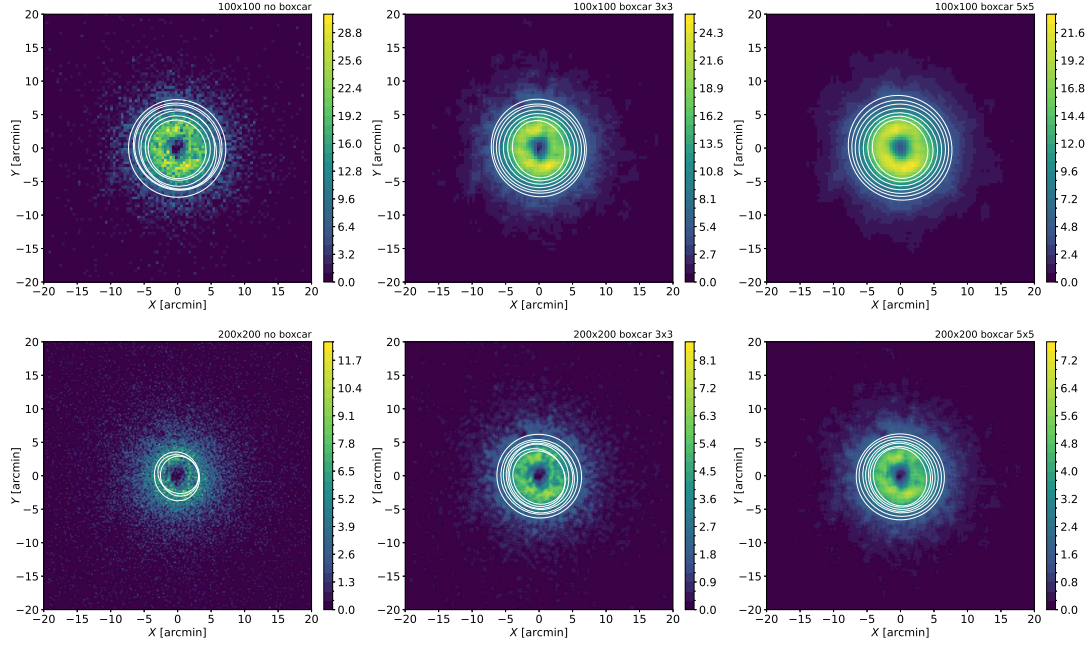


Fig. 4: Ellipse fitting results for all considered 38 stellar density intervals within the $40' \times 40'$ field. From left to right the first row presents the 100×100 array under the three conditions – unsmoothed, 3×3 boxcar and 5×5 boxcar. The second row shows the same arrangement for the 200×200 array. The color scale on the right of the panels represents the density \ast / px .

3.2 Structural parameters obtained via discrete MCMC sampling

We also derive the structural parameters of the GC M 15 – the central coordinates (X_C, Y_C), the PA and the ellipticity ϵ by fitting a 2D Plummer model, using a modified version of the discrete maximum likelihood method³. For more details, see Kacharov et al. (2014). This method utilizes the discrete source distribution within the cluster and determines the most probable parameters through MCMC optimization.

The input data consist of the filtered samples for the various field sizes after the subtraction of one of the two background estimates, totaling 50 datasets (5 filters \times 5 field sizes \times 2 background fields). We analyzed additional 25 datasets (5 filters \times 5 field sizes) without background subtraction. In total, 75 independent tests were conducted. The results are presented in Table A.2, where column 2 presents the four types of filtration (f1–f4) and f0 designates unfiltered samples. The various types of background subtraction are listed in column 3: b1 and b2 indicate the two different background fields that were used for subtraction, b0 marks no background subtraction.

Our MCMC analysis used a characteristic radius of $r_s = 4'.5$, chosen because interior to this point, both the sample completeness and photometric accuracy are significantly decreased by stellar crowding. In this implementation, the python module EMCEE MCMC algorithm (Foreman-Mackey et al. 2013) was initialized with 40 walkers for each parameter, then each of the 40 chains was run for 600 steps. The posterior distribution for each parameter was constructed from the values of the last 150 steps of each of the 40 walkers (6 000 values total). The best-fit value for each parameter was taken as the median (the 0.5 quantile) of its distribution. The uncertainties were estimated from the 0.25 and 0.75 quantiles. Figure 5 shows an example of a corner plot illustrating the correlations between the derived parameters, with contours representing the probability distributions.

³ https://github.com/kacharov/morphology_2d

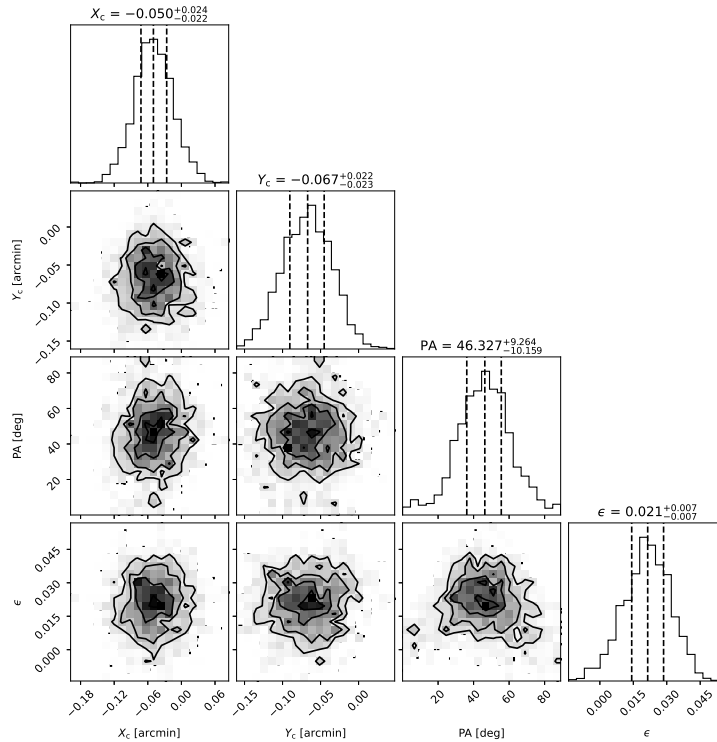


Fig. 5: Example of M 15 structural parameters derived from MCMC for $50' \times 50'$ field using filtration f3 and background subtraction b2. The histograms show the distribution for each parameter, with vertical dashed lines marking the 0.25, 0.5, and 0.75 quantiles. The contour plots show the pairwise parameter correlations. The median values and corresponding errors are listed above each histogram.

4 RESULTS AND DISCUSSION

In this section, we present our results for the structural parameters of the GC M 15 and compare them with those proposed by other authors.

Figure 6 illustrates the agreement between the cluster center coordinates determined in our work and these from Goldsbury et al. (2010). The figure shows the offsets ΔX_C and ΔY_C (in arcmin) for the centers of 38 ellipses fitted to the smoothed stellar number density. Their weighted mean and standard deviation are $\Delta X_C = -0'.013 \pm 0'.094$ and $\Delta Y_C = -0'.067 \pm 0'.129$, respectively.

Given that our centers are derived from the stellar density in the regions outside the cluster core – whereas the literature center is typically defined by the average coordinates of the brightest stars clustered in the innermost region – the two definitions are not expected to coincide a priori. Our results show that the mean center of the fitted ellipses is offset by a distance of $\sim 0'.068$, or $4''.1 \pm 9''.6$. This represents an excellent agreement, with the uncertainty being on the order of the resolution of our density maps ($12''$ – $24''$).

The results from the MCMC method show weighted mean offsets $\Delta X_C = -0'.069 \pm 0'.056$ and $\Delta Y_C = -0'.071 \pm 0'.023$ or the total offset is $5''.9 \pm 3''.6$ south-eastward from the adopted center value. Although the MCMC method provides a formally more precise determination of the M 15 central coordinates (as indicated by the smaller statistical uncertainties), its result shows a larger deviation from the literature value of Goldsbury et al. (2010).

In Figure 7, the results for the ellipticity are combined as a function of cluster-centric distance, R . Mean values are calculated for two regions: $R \leq 4'.5$ and $R > 4'.5$. This figure indicates a radial varia-

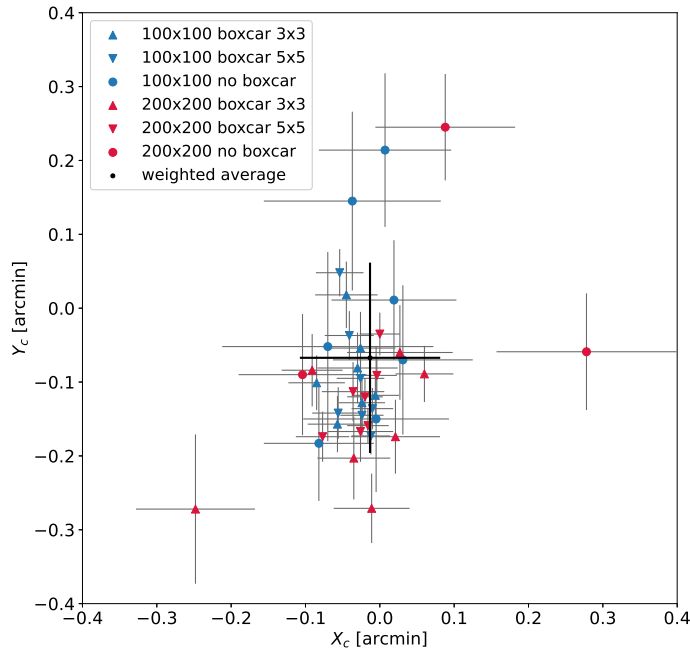


Fig. 6: M 15 Center coordinates derived from 38 ellipses of different stellar densities with their weighted mean and standard deviation: $\Delta X_C = -0'.013 \pm 0'.094$ and $\Delta Y_C = -0'.067 \pm 0'.129$, respectively. The mean is displaced by $\sim 0'.068$ or $4''.1 \pm 9''.6$ relative to the adopted center coordinates of M 15 from Goldsbury et al. (2010).

tion in the ellipticity of M 15. The mean value is $\epsilon = 0.09 \pm 0.02$ for the inner region and 0.04 ± 0.02 for the outer region of the cluster. Bianchini et al. (2013) reveal that M 15 exhibits a steep rotation profile that diminishes rapidly in the cluster’s periphery. Specifically, systemic rotation becomes negligible at radial distances beyond 4–5 arcmin. This lack of rotational support likely accounts for the reduced ellipticity observed in the cluster’s outskirts, where the morphology becomes increasingly spherical.

Crucially, this specific kinematic and morphological structure places important constraints on the cluster’s formation history. While standard in-situ GCs are expected to lose significant angular momentum through long-term dynamical relaxation, becoming largely pressure-supported and spherical, M 15 retains a rapidly rotating core. Such a combination of high central rotation and strong central concentration is physically consistent with expectations for the stripped nuclei of dwarf galaxies, whose deep potential wells can preserve internal rotation over long timescales. Therefore, our detection of a pronounced ellipticity gradient from a rotationally-flattened core to a relaxed, spherical halo provides morphological support for the hypothesis that M 15 is the remnant nucleus of a disrupted satellite galaxy, rather than a classical in-situ cluster. This evidence is particularly valuable given the ambiguity in M 15’s current classification. We note that Belokurov & Kravtsov (2024) formally classify M 15 as in-situ based on its orbital energy and location within the central 10 kpc ($R_{GC} \approx 10.4$ kpc, Harris 1996, 2010 edition), but they explicitly flag it as a borderline case due to its enhanced [Eu/Fe] abundance. This distinction is further clarified by Monty et al. (2024), whose analysis confirms that among the other GC M 15 shows the highest [Eu/ α] abundance, indicating a chemical enrichment history distinct from that of the Milky Way. Consequently, our structural analysis reinforces the scenario that M 15 is an accreted nucleus that has settled into the inner halo.

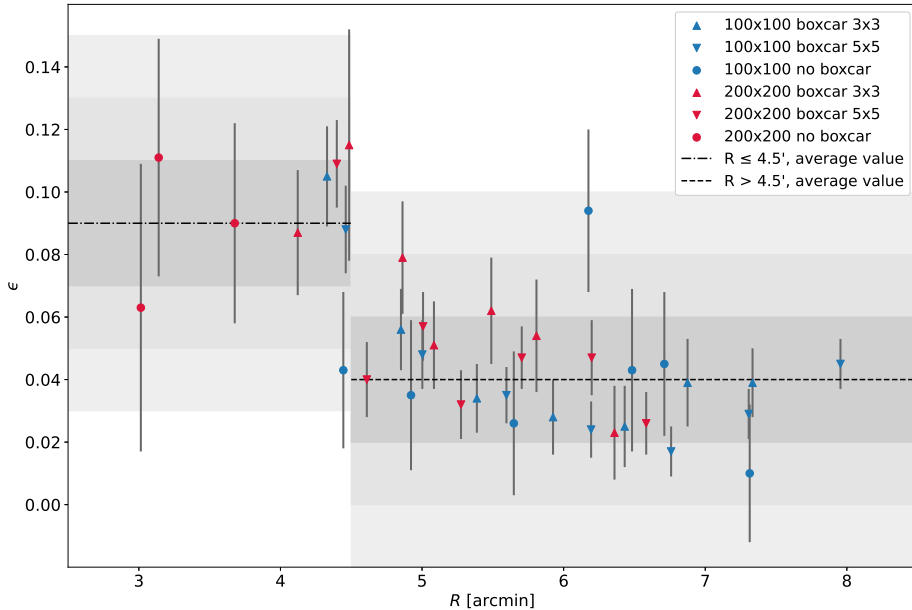


Fig. 7: Ellipticities ϵ of the 38 fitted ellipses at various radii. The mean ϵ values in the radial intervals $3'.0 < R \leq 4'.5$ and $4'.5 < R < 8'.0$ are 0.09 ± 0.02 and 0.04 ± 0.02 , respectively. The dark, medium, and light grey shaded regions correspond to the $\pm 1\sigma$, $\pm 2\sigma$, and $\pm 3\sigma$ intervals.

Figure 8 compares our ellipticity results for $R > 4'.5$, derived from boxcar-smoothed stellar densities, with the findings of White & Shawl (1987). Our results are in contradiction with theirs in the region $4'.9 < R < 6'$. Given that the errors on the ellipticities measured by White & Shawl (1987) are ~ 0.03 , this difference is most significant at $R = 5'.3$, reaching a level of $\sim 3\sigma$. Our measured ellipticities are also inconsistent with the value from Chen & Chen (2010), but a similar discrepancy was also found by Botev et al. (2025) for the GC M 2. In contrast, our result is in excellent agreement with the finding of Cruz Reyes & Anderson (2024), who reported $\epsilon = 0.039 \pm 0.009$ at $R = 7'.5$.

We applied our ellipse fitting technique using recent Gaia EDR3 data provided by Vasiliev & Baumgardt (2021) and already utilized by Cruz Reyes & Anderson (2024), in order to check whether the ellipticity varies with the distance from the center of M 15. The sample contains 19770 member stars and we measured 67 ellipticities within the range of $3' < R < 7'.5$ by fitting the smoothed number densities (see Figure 8). It is evident that the variation of the ellipticity is in good agreement with our results based on PS1 DR2, confirming lower ellipticity in the outer regions ($R > 4'.5$) of M 15 in comparison to the inner regions ($R < 4'.5$).

The MCMC analysis yields a weighted average ellipticity of $\epsilon = 0.022 \pm 0.005$ (see Figure 9), which is representative of the entire cluster and agrees well with the ellipticities determined from ellipse fitting in the outer regions. However, considering the incompleteness of the samples in the central regions and the effects of stellar crowding, a single ellipticity value is likely insufficient to accurately represent the overall oblateness of the GC M 15.

We find that the PA, as determined by the ellipse fitting of the stellar number density, can be assumed as a constant value: $PA = 44^\circ.4 \pm 16^\circ.2$. The standard deviation is slightly affected by the weak radial trend of increasing PA with cluster-centric distance (see Figure 10).

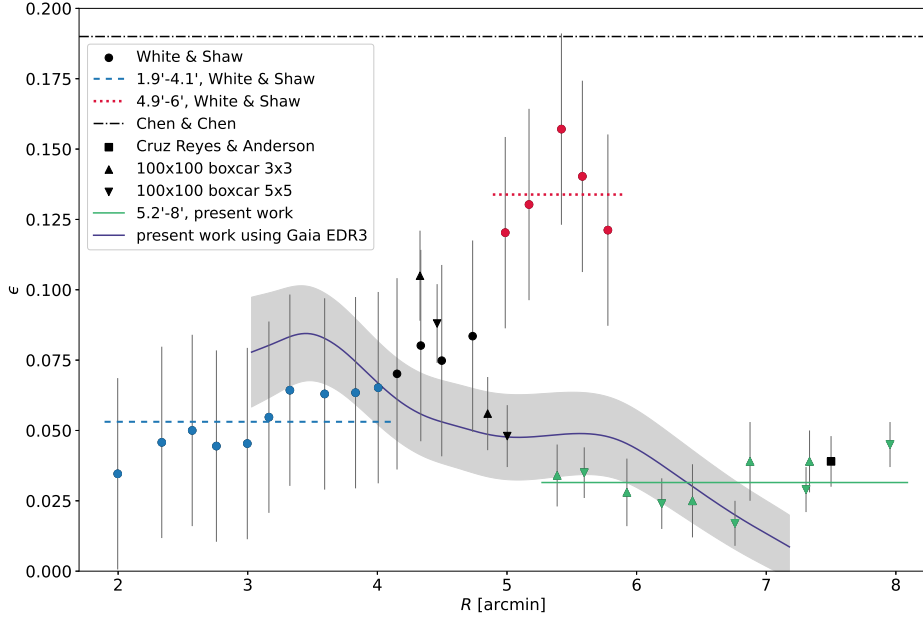


Fig. 8: Comparison of the ellipticity derived in this work with those reported in previous studies. The measurements of White & Shaw (1987) are denoted with dots; the blue dashed line marks their mean value of 0.05 ± 0.01 for radii between $1'.9$ and $4'.1$, and the red dotted line indicates 0.13 ± 0.02 for radii between $4'.9$ and $6'$. The data points used to compute these averages are shown in the corresponding colors. The mean ellipticity reported by Chen & Chen (2010) is shown as a black dash-dotted line and the black square represents the value measured by Cruz Reyes & Anderson (2024). The triangles indicate our results based on PS1 DR2 data and the green solid line corresponds to the mean value of 0.03 ± 0.01 for the subset of our data highlighted in green. Alternatively, we perform 73 measurements by ellipse fitting of the smoothed number densities based on Gaia EDR3 data (Vasiliev & Baumgardt 2021). The purple solid line and the grey shaded region show the variation of ellipticity within $\pm 1\sigma$ interval.

The result from the MCMC method for the $PA = 46^\circ 6 \pm 7^\circ 1$ (see Figure 9) is in excellent agreement with the value from the ellipse fitting. Cruz Reyes & Anderson (2024) reported $PA = 119^\circ 2 \pm 19^\circ 6$ at $R = 7'.5$, which was measured with respect to West instead of North. Correcting for this offset, their value would be $29^\circ 2 \pm 19^\circ 6$, which is consistent with our results within 1σ .

The comparison of the structural parameters from this work and other studies is summarized in Table 1 and Table 2.

5 CONCLUSIONS

This study of the M15 is based on 38 stellar density intervals, derived from photometric data from the PS1 DR2 catalog (Flewellling et al. 2020). Our study focuses on the estimation of the structural parameters (center coordinates, ellipticity, and PA) of this GC via ellipse fitting and a 2D Plummer profile fit to its overall discrete stellar density distribution, using a maximum likelihood approach.

By applying several specific filtering techniques, we confirm the findings of Botev et al. (2025) that the averaged 2D distributions of the smoothed number density yield more accurate results for the

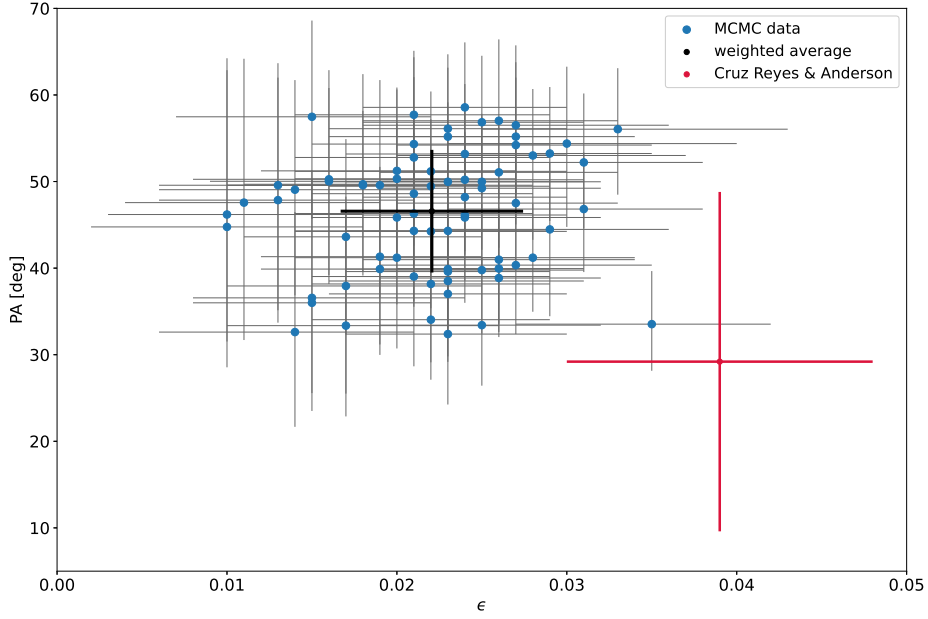


Fig. 9: Results of the 75 MCMC fits (see Table A.2) to the structural parameters of M 15 – ellipticity (abscissa) and position angle (ordinate), and their weighted mean values and standard deviations: $\epsilon = 0.022 \pm 0.005$ and $PA = 46.6 \pm 7.1$, respectively.

Table 1: Comparison of Position Angles Presented in This Work and Those Reported in Previous Studies.

PA [deg]	PA err [deg]	References
29.2	19.6	Cruz Reyes & Anderson (2024)
36.1	2.9	Martens et al. (2023)
76.6	12.1	Sollima et al. (2019)
35	1	White & Shawl (1987)
44.4	16.2	present work (ellipse fitting)
46.6	7.1	present work (MCMC method)

Table 2: Comparison of Ellipticities ϵ from This Paper with Other Studies Measured at Different Distances R from the GC Center.

ϵ	ϵ err	R [']	References
0.19	0.1	-	Chen & Chen (2010)
0.039	0.009	7.5	Cruz Reyes & Anderson (2024)
0.05	0.01	1.9–4.1	White & Shawl (1987)
0.13	0.02	4.9–6.0	White & Shawl (1987)
0.09	0.02	3.0–4.5	present work (ellipse fitting)
0.04	0.02	4.5–8.0	present work (ellipse fitting)
0.022	0.005	-	present work (MCMC method)

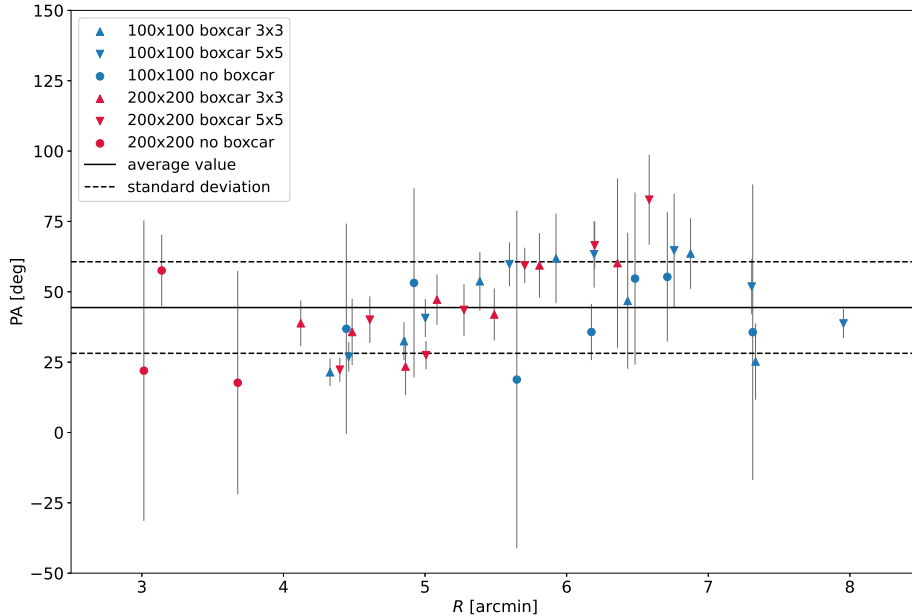


Fig. 10: Position angles of the 38 fitted ellipses with a mean value marked by a solid black line and a standard deviation indicated by dashed lines: $PA = 44^\circ.4 \pm 16^\circ.2$.

structural parameters of GCs than the discrete number density. We also find that the photometric quality flags serve as an important discriminator for the PS1 DR2 data samples. The results, based on the analysis of different photometric bands and angular scales, are in good agreement.

We find a radial variation in the ellipticity of M 15, which decreases from a mean value of $\epsilon = 0.09 \pm 0.02$ at cluster-centric distances $R \leq 4'.5$ to 0.04 ± 0.02 at $R > 4'.5$ (1σ confidence level). The latter value is in excellent agreement with the result of Cruz Reyes & Anderson (2024), who found $\epsilon = 0.039 \pm 0.009$ at $R = 7'.5$. Theoretically, ellipticity is expected to increase in the outer region, because it is generally more susceptible to elongation due to tidal effects, while the inner region has a faster relaxation time, which acts towards decreasing anisotropy and increasing sphericity. However, the significant rotation of M 15, characterized by the steep profile presented by Bianchini et al. (2013) (see their Figure 10), provides a mechanism for the observed core ellipticity. The relatively low ellipticity in the outer region suggests that there is no significant stellar tidal stripping in M 15 at $R \sim 8'$.

The results from the discrete MCMC fit show an ellipticity of $\epsilon = 0.022 \pm 0.005$, representative of the entire cluster, which also agrees well with the ellipticities determined from ellipse fitting in the outer regions. However, considering the incompleteness of the samples in the central regions and the effects of stellar crowding, a single ellipticity value is likely insufficient to accurately represent the overall oblateness of M 15.

The mean offsets of the centers of all isodensity fitted ellipses are $\Delta\alpha = +0'.013$ and $\Delta\delta = -0'.067$, corresponding to a distance of $4''.1 \pm 9''.6$ from the previously precisely measured coordinates (Goldsbury et al. 2010) of the M 15 center. This offset is on the order of the resolution of our maps ($12''$ – $24''$).

We determine that the position angle, derived from the ellipse fitting of the stellar density, can be considered as nearly constant: $PA = 44^\circ.4 \pm 16^\circ.2$. The result obtained from the MCMC method, $PA = 46^\circ.6 \pm 7^\circ.1$, is in excellent agreement with the ellipse fitting result.

Acknowledgements The research that led to these results was partially carried out with the help of infrastructure purchased under the National Roadmap for Research Infrastructure, financially coordinated by the Ministry of Education and Science of Republic of Bulgaria (D01-109/30.06.2025).

The Pan-STARRS1 Surveys (PS1) and the PS1 public science archive have been made possible through contributions by the Institute for Astronomy, the University of Hawaii, the Pan-STARRS Project Office, the Max-Planck Society and its participating institutes, the Max Planck Institute for Astronomy, Heidelberg and the Max Planck Institute for Extraterrestrial Physics, Garching, The Johns Hopkins University, Durham University, the University of Edinburgh, the Queen's University Belfast, the Harvard-Smithsonian Center for Astrophysics, the Las Cumbres Observatory Global Telescope Network Incorporated, the National Central University of Taiwan, the Space Telescope Science Institute, the National Aeronautics and Space Administration under Grant No. NNX08AR22G issued through the Planetary Science Division of the NASA Science Mission Directorate, the National Science Foundation Grant No. AST-1238877, the University of Maryland, Eotvos Lorand University (ELTE), the Los Alamos National Laboratory, and the Gordon and Betty Moore Foundation.

Appendix A: SUPPLEMENTARY DATA

This appendix presents the supplementary tables referenced in the main text. Table A1 contains the complete data obtained by ellipse fitting of the 2D stellar number isodensity distribution, while Table A2 lists the full derived structural parameters from MCMC.

Table A.1: Ellipse Parameters Estimated from the Unfiltered $40' \times 40'$ Sample under Varying Stellar Densities, Star Counting and Smoothing Techniques (see Section 3.1 for details).

image size [px×px]	boxcar [px×px]	density [*px]	X_C [']	err [']	Y_C [']	err [']	a [']	err [']	b [']	err [']	PA [deg]	err [deg]	ϵ	err
100×100	-	6	-0.07	0.142	-0.052	0.128	7.314	0.118	7.239	0.126	35.621	52.528	0.01	0.022
100×100	-	7-8	0.007	0.089	0.214	0.104	6.711	0.093	6.408	0.11	55.286	22.983	0.045	0.023
100×100	-	8-9	-0.037	0.119	0.145	0.121	6.483	0.118	6.208	0.119	54.703	30.57	0.043	0.026
100×100	-	9-10	-0.005	0.098	-0.15	0.099	6.175	0.12	5.594	0.097	35.72	9.993	0.094	0.026
100×100	-	10-12	0.031	0.094	-0.07	0.101	5.648	0.094	5.503	0.091	18.801	59.981	0.026	0.023
100×100	-	12-14	0.019	0.084	0.011	0.081	4.922	0.086	4.752	0.083	53.159	33.629	0.035	0.024
100×100	-	14-17	-0.082	0.074	-0.183	0.078	4.444	0.081	4.255	0.079	36.85	37.377	0.043	0.025
100×100	3×3	5.0-6.0	-0.045	0.042	0.018	0.045	7.334	0.056	7.047	0.049	25.22	13.564	0.039	0.011
100×100	3×3	6.0-7.0	-0.03	0.054	-0.081	0.048	6.875	0.065	6.606	0.054	63.584	12.537	0.039	0.014
100×100	3×3	7.0-8.0	-0.026	0.047	-0.054	0.049	6.431	0.053	6.268	0.053	46.806	24.169	0.025	0.013
100×100	3×3	8.0-9.5	-0.085	0.038	-0.101	0.037	5.925	0.045	5.762	0.042	61.875	15.922	0.028	0.012
100×100	3×3	9.5-12.0	-0.006	0.032	-0.118	0.03	5.387	0.037	5.205	0.037	53.736	10.375	0.034	0.011
100×100	3×3	12.0-15.0	-0.024	0.031	-0.128	0.033	4.851	0.039	4.581	0.039	32.44	6.755	0.056	0.013
100×100	3×3	15.0-18.0	-0.057	0.04	-0.157	0.038	4.329	0.041	3.876	0.049	21.395	4.925	0.105	0.016
100×100	5×5	4.0-5.0	-0.054	0.032	0.048	0.032	7.955	0.044	7.599	0.035	38.733	5.119	0.045	0.008
100×100	5×5	5.0-6.0	-0.041	0.033	-0.037	0.033	7.307	0.041	7.094	0.036	51.853	9.871	0.029	0.008
100×100	5×5	6.0-7.0	-0.026	0.032	-0.095	0.03	6.759	0.035	6.648	0.034	64.685	20.231	0.017	0.008
100×100	5×5	7.0-9.0	-0.024	0.029	-0.145	0.027	6.194	0.035	6.045	0.031	63.336	11.843	0.024	0.009
100×100	5×5	9.0-11.0	-0.012	0.026	-0.173	0.025	5.596	0.031	5.403	0.031	59.814	7.756	0.035	0.009
100×100	5×5	11.0-14.0	-0.01	0.028	-0.136	0.028	5.002	0.034	4.763	0.036	40.688	6.758	0.048	0.011
100×100	5×5	14.0-17.0	-0.056	0.035	-0.142	0.035	4.461	0.04	4.068	0.044	26.852	5.195	0.088	0.014
200×200	-	6	-0.104	0.086	-0.09	0.082	3.677	0.08	3.347	0.085	17.68	39.712	0.09	0.032
200×200	-	7	0.088	0.094	0.245	0.072	3.14	0.09	2.791	0.083	57.57	12.681	0.111	0.038
200×200	-	8-9	0.278	0.121	-0.059	0.079	3.014	0.071	2.823	0.125	21.951	53.364	0.063	0.046
200×200	3×3	2.0-2.1	0.027	0.071	-0.06	0.064	6.359	0.072	6.214	0.064	60.173	30.108	0.023	0.015
200×200	3×3	2.3-2.4	0.021	0.06	-0.174	0.05	5.808	0.071	5.495	0.063	59.375	11.491	0.054	0.018
200×200	3×3	2.6-2.8	-0.035	0.049	-0.203	0.056	5.489	0.07	5.149	0.052	41.934	9.217	0.062	0.017
200×200	3×3	3.0-3.2	0.06	0.039	-0.089	0.038	5.084	0.048	4.825	0.045	47.223	8.938	0.051	0.014
200×200	3×3	3.4-3.6	-0.091	0.041	-0.084	0.049	4.862	0.057	4.48	0.053	23.446	10.155	0.079	0.018
200×200	3×3	3.8-4.0	-0.248	0.08	-0.272	0.101	4.485	0.119	3.968	0.098	35.711	11.758	0.115	0.037
200×200	3×3	4.2-4.4	-0.011	0.051	-0.271	0.047	4.122	0.05	3.763	0.061	38.808	8.14	0.087	0.02
200×200	5×5	1.7-1.8	-0.026	0.044	-0.167	0.041	6.583	0.049	6.414	0.041	82.714	15.975	0.026	0.01
200×200	5×5	2.0-2.1	-0.036	0.042	-0.113	0.04	6.198	0.05	5.907	0.044	66.495	8.322	0.047	0.012
200×200	5×5	2.3-2.5	0.0	0.027	-0.035	0.029	5.704	0.033	5.438	0.036	59.372	6.292	0.047	0.01
200×200	5×5	2.7-2.9	-0.02	0.024	-0.12	0.025	5.275	0.035	5.108	0.031	43.554	9.18	0.032	0.011
200×200	5×5	3.1-3.3	-0.004	0.027	-0.091	0.024	5.007	0.032	4.721	0.035	27.474	5.024	0.057	0.011
200×200	5×5	3.5-3.7	-0.016	0.028	-0.159	0.024	4.61	0.027	4.425	0.035	40.082	8.276	0.04	0.012
200×200	5×5	3.9-4.1	-0.077	0.036	-0.174	0.034	4.398	0.04	3.919	0.042	22.297	4.275	0.109	0.014

Table A.2: MCMC Obtained Structural Parameters for Samples with Different Field Sizes, Filtering Conditions, and Background Subtraction Methods (see Section 3.2 for details).

image size	filtration type	background subtraction	X_C [']	err [']	Y_C [']	err [']	PA [deg]	err [deg]	ϵ	err	Number of stars
20' × 20'	f0	b0	-0.033	0.02	-0.117	0.019	33.53	6.131	0.035	0.008	18515
20' × 20'	f0	b1	-0.125	0.024	-0.074	0.024	56.505	9.225	0.027	0.009	11278
20' × 20'	f0	b2	-0.108	0.027	-0.092	0.029	54.385	9.626	0.030	0.010	10997
20' × 20'	f1	b0	0.007	0.024	-0.099	0.022	38.514	10.886	0.023	0.008	14303
20' × 20'	f1	b1	0.007	0.023	-0.085	0.026	45.848	9.855	0.024	0.008	13088
20' × 20'	f1	b2	-0.004	0.023	-0.117	0.027	40.348	9.167	0.027	0.008	12845
20' × 20'	f2	b0	-0.169	0.027	-0.081	0.027	53.01	9.74	0.028	0.009	13187
20' × 20'	f2	b1	-0.156	0.026	-0.065	0.023	56.047	7.563	0.033	0.010	12028
20' × 20'	f2	b2	-0.158	0.026	-0.087	0.025	52.208	7.964	0.031	0.008	11799
20' × 20'	f3	b0	-0.044	0.025	-0.103	0.022	40.978	8.995	0.026	0.008	14919
20' × 20'	f3	b1	-0.034	0.020	-0.084	0.022	46.822	7.277	0.031	0.008	13670
20' × 20'	f3	b2	-0.051	0.021	-0.105	0.023	44.473	10.027	0.029	0.007	13414
20' × 20'	f4	b0	-0.126	0.027	-0.082	0.023	49.573	12.949	0.019	0.009	12571
20' × 20'	f4	b1	-0.107	0.026	-0.078	0.030	57.021	9.397	0.026	0.008	11444
20' × 20'	f4	b2	-0.120	0.029	-0.101	0.028	54.213	9.568	0.027	0.008	11235
30' × 30'	f0	b0	-0.032	0.019	-0.103	0.019	33.415	7.85	0.025	0.007	22332
30' × 30'	f0	b1	-0.092	0.025	-0.053	0.025	49.974	11.688	0.023	0.008	12884
30' × 30'	f0	b2	-0.087	0.031	-0.090	0.029	56.104	8.594	0.023	0.007	12201
30' × 30'	f1	b0	0.002	0.02	-0.086	0.025	36.566	14.725	0.015	0.009	17793
30' × 30'	f1	b1	-0.007	0.025	-0.074	0.024	48.598	9.110	0.021	0.007	14948
30' × 30'	f1	b2	0.003	0.021	-0.097	0.020	44.301	9.053	0.021	0.007	14371
30' × 30'	f2	b0	-0.156	0.03	-0.064	0.024	49.687	12.72	0.018	0.007	16612
30' × 30'	f2	b1	-0.141	0.024	-0.041	0.025	58.568	9.053	0.024	0.006	13883
30' × 30'	f2	b2	-0.125	0.023	-0.095	0.030	53.239	7.792	0.029	0.007	13320
30' × 30'	f3	b0	-0.04	0.022	-0.079	0.023	38.171	9.11	0.022	0.007	18504
30' × 30'	f3	b1	-0.040	0.021	-0.076	0.021	48.197	7.506	0.024	0.006	15591
30' × 30'	f3	b2	-0.034	0.022	-0.096	0.023	47.510	7.792	0.027	0.007	14980
30' × 30'	f4	b0	-0.12	0.026	-0.058	0.025	46.192	17.647	0.01	0.008	15901
30' × 30'	f4	b1	-0.099	0.028	-0.059	0.023	55.188	8.537	0.023	0.007	13244
30' × 30'	f4	b2	-0.088	0.027	-0.090	0.026	49.974	9.683	0.025	0.008	12706
40' × 40'	f0	b0	-0.018	0.018	-0.106	0.016	37.025	7.907	0.023	0.007	25719
40' × 40'	f0	b1	-0.013	0.019	-0.088	0.020	39.947	7.047	0.026	0.006	19802
40' × 40'	f0	b2	-0.024	0.022	-0.107	0.022	41.207	6.245	0.028	0.006	18360
40' × 40'	f1	b0	0.005	0.021	-0.077	0.024	33.358	13.121	0.017	0.009	20794
40' × 40'	f1	b1	0.006	0.022	-0.050	0.021	45.848	10.829	0.020	0.007	15600
40' × 40'	f1	b2	-0.004	0.023	-0.068	0.024	39.603	8.308	0.023	0.006	14576
40' × 40'	f2	b0	-0.147	0.023	-0.067	0.026	49.573	9.912	0.018	0.008	19499
40' × 40'	f2	b1	-0.142	0.026	-0.048	0.024	53.182	8.079	0.024	0.007	14501
40' × 40'	f2	b2	-0.133	0.026	-0.069	0.026	51.062	8.709	0.026	0.007	13496
40' × 40'	f3	b0	-0.036	0.024	-0.082	0.025	39.03	10.371	0.021	0.008	21596
40' × 40'	f3	b1	-0.032	0.023	-0.049	0.022	50.203	8.652	0.024	0.007	16279
40' × 40'	f3	b2	-0.044	0.024	-0.072	0.023	46.135	7.563	0.024	0.006	15196
40' × 40'	f4	b0	-0.115	0.023	-0.058	0.03	47.854	14.152	0.013	0.008	18697
40' × 40'	f4	b1	-0.093	0.025	-0.039	0.023	51.234	9.626	0.02	0.008	13820
40' × 40'	f4	b2	-0.092	0.027	-0.061	0.024	49.229	8.594	0.025	0.007	12878
50' × 50'	f0	b0	-0.024	0.017	-0.095	0.018	32.384	8.136	0.023	0.007	29757
50' × 50'	f0	b1	-0.009	0.017	-0.079	0.021	39.89	7.735	0.023	0.006	20444
50' × 50'	f0	b2	-0.019	0.02	-0.096	0.021	38.858	7.162	0.026	0.007	18188
50' × 50'	f1	b0	0.006	0.023	-0.091	0.024	35.993	14.324	0.015	0.007	24362
50' × 50'	f1	b1	0.013	0.023	-0.05	0.022	43.614	11.287	0.017	0.008	16150
50' × 50'	f1	b2	-0.015	0.025	-0.061	0.025	41.322	10.371	0.019	0.007	14485
50' × 50'	f2	b0	-0.148	0.024	-0.064	0.025	50.031	10.829	0.016	0.007	22895
50' × 50'	f2	b1	-0.131	0.022	-0.03	0.025	55.188	6.818	0.027	0.007	15054
50' × 50'	f2	b2	-0.132	0.027	-0.06	0.027	49.458	8.422	0.022	0.007	13394
50' × 50'	f3	b0	-0.032	0.021	-0.078	0.022	37.941	12.433	0.017	0.008	25236
50' × 50'	f3	b1	-0.028	0.022	-0.068	0.024	50.317	10.313	0.02	0.007	16851
50' × 50'	f3	b2	-0.05	0.024	-0.067	0.023	46.327	10.159	0.021	0.007	15097
50' × 50'	f4	b0	-0.109	0.025	-0.058	0.028	44.76	19.481	0.01	0.008	22021
50' × 50'	f4	b1	-0.082	0.025	-0.031	0.025	56.849	8.48	0.025	0.007	14355
50' × 50'	f4	b2	-0.095	0.027	-0.035	0.021	52.781	10.199	0.021	0.008	12784
60' × 60'	f0	b0	-0.026	0.018	-0.103	0.021	34.045	7.678	0.022	0.007	34502
60' × 60'	f0	b1	-0.011	0.02	-0.088	0.02	44.301	7.678	0.023	0.006	20895
60' × 60'	f0	b2	-0.011	0.022	-0.075	0.02	39.775	7.62	0.025	0.006	17577
60' × 60'	f1	b0	0.01	0.022	-0.079	0.022	32.613	13.866	0.014	0.008	28570
60' × 60'	f1	b1	0.009	0.025	-0.056	0.022	47.567	16.616	0.011	0.008	16569
60' × 60'	f1	b2	0.005	0.025	-0.046	0.022	41.207	10.485	0.02	0.007	14064
60' × 60'	f2	b0	-0.148	0.023	-0.066	0.022	50.26	12.605	0.016	0.008	26906
60' × 60'	f2	b1	-0.139	0.028	-0.019	0.025	57.709	9.11	0.021	0.008	15439
60' × 60'	f2	b2	-0.118	0.027	-0.031	0.022	51.177	9.912	0.022	0.008	12957
60' × 60'	f3	b0	-0.032	0.023	-0.083	0.021	39.89	9.912	0.019	0.008	29532
60' × 60'	f3	b1	-0.037	0.018	-0.051	0.022	49.057	12.662	0.014	0.008	17281
60' × 60'	f3	b2	-0.027	0.026	-0.047	0.024	44.244	9.053	0.022	0.008	14669
60' × 60'	f4	b0	-0.108	0.03	-0.064	0.025	49.573	14.439	0.013	0.008	25944
60' × 60'	f4	b1	-0.102	0.027	-0.021	0.021	57.479	11.803	0.015	0.008	14709
60' × 60'	f4	b2	-0.086	0.027	-0.028	0.029	54.328	10.027	0.021	0.008	12366

Appendix B: TESTING THE EFFECTS OF BOXCAR SMOOTHING ON ELLIPTICITY MEASUREMENTS

To ensure that the pixel-binning and subsequent boxcar smoothing procedure utilized in our methodology does not introduce any systematic bias into the derived structural parameters, we performed a series of validation tests using mock stellar density maps. Following the approach used for the observational data, we generated synthetic 2D Plummer number density distributions with a predefined range of constant ellipticities, covering different input values in the interval from 0.01 to 0.5. These mock images were constructed to simulate the spatial resolution and typical noise characteristics of our actual density maps. We then analyzed these mock images with our ellipse-fitting algorithm in two ways: first on the raw, unsmoothed pixel-binned maps, and second on the maps after applying the exact same boxcar smoothing kernel described in Section 3.1. The results of this validation are presented in Figure B.1. The two leftmost panels display the measured ellipticities obtained from the unsmoothed mock maps as a function of radius R . As expected, the inherent pixel noise introduces a noticeable scatter around the true input values. Conversely, the middle and right panels show the measurements obtained after applying our boxcar smoothing kernel. It is clearly visible that the smoothing process significantly reduces the scatter, aligning the measured ellipticities with the true input values. Therefore, we conclude that the applied boxcar smoothing process effectively reduces local pixel noise and improves the precision of the measurement, without artificially dampening, enhancing, or otherwise biasing the ellipticity of the cluster's isodensity contours.

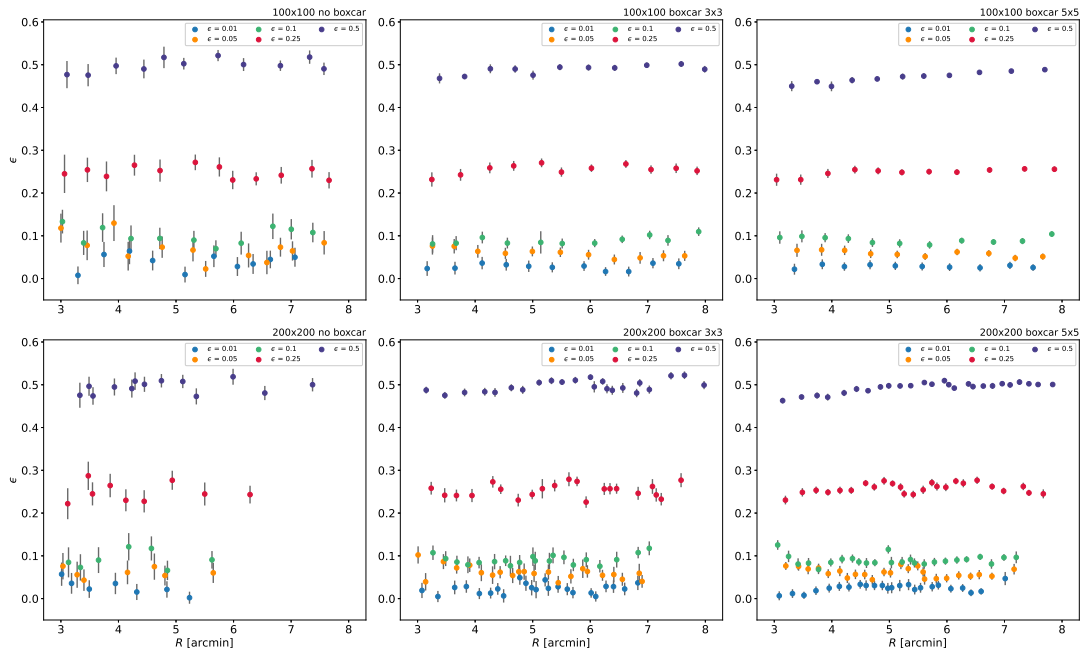


Fig. B.1: Ellipticities derived from mock stellar density maps as a function of radius R . The mock maps were generated with ellipticities 0.01 (blue), 0.05 (orange), 0.1 (green), 0.25 (red), 0.5 (purple) and a constant PA = 45° along the radial distance R . From left to right the first row presents the 100×100 array under the three conditions – unsmoothed (left), 3×3 boxcar (middle) and 5×5 boxcar (right). The second row shows the same arrangement for the 200×200 array.

References

- Baumgardt H., Hénault-Brunet V., Dickson N., & Sollima A., 2023, *MNRAS*, 521, 3991 2
- Bianchini P., Varri A. L., Bertin G., & Zocchi A., 2013, *ApJ*, 772, 67 8, 12
- Belokurov V., Kravtsov A., 2024, *MNRAS*, 528, 3198 2, 8
- Botev S., Petrov G., Valcheva A., Nedialkov P., 2025, *Phys*, 100, 075005 2, 9, 10
- Chen C. W., & Chen W. P., 2010, *ApJ*, 721, 1790 1, 9, 10, 11
- Chen Y., Gnedin O. Y., Price-Whelan A. M., & Holm-Hansen C., 2025, *ApJ*, 995, 15 2
- Cruz Reyes M., & Anderson I. R., 2024, *A&A*, 689, A232 1, 9, 10, 11, 12
- Efron B., 1979, *Ann. Statist.*, 7, 1 Jan., 1 5
- Flewelling H. A., Magnier E. A., Chambers K. C. et al., 2020, *ApJS*, 251, 7 2, 3, 10
- Foreman-Mackey D., Hogg D. W., Lang D., & Goodman J., 2013, *PASP*, 125, 306 6
- Garro E. R., Minniti D., & Fernández-Trincado J. G., 2024, *A&A*, 687, A214 1
- Goldsbury R., Richer H. B., Anderson J. et al., 2010, *AJ*, 140, 1830 2, 3, 7, 8, 12
- Gerssen J., van der Marel R. P., Gebhardt K. et al., 2002, *AJ*, 124, 3270 2
- Harris W. E. 1996, *AJ*, 112, 1487 1, 2, 8
- Huang Y., Li Q., Liu J. et al., 2025, *NSRev*, 12, 347 2
- Kacharov N., Bianchini P., Koch A. et al., 2014, *A&A*, 567, A69 6
- Lee J.-W., & Carney B. W., 1999, *AJ*, 117, 2868 3
- Martens S., Kamann S., Dreizler S. et al., 2023, *A&A*, 671, A106, Cat. J/A+A/671/A106 11
- Monty S., Belokurov V., Sanders J. L. et al., 2024, *MNRAS*, 533, 2420 8
- Sollima A., Baumgardt H., & Hilker M., 2019, *MNRAS*, 485, 1460 11
- van der Walt S., Schönberger J.L., Nunez-Iglesias J., et al., 2014, *PeerJ*:e453 5
- Vasiliev E., & Baumgardt H., 2021, *MNRAS*, 505, 5978 9, 10
- White, R. E., & Shawl, S. J., 1987, *ApJ*, 317, 246 9, 10, 11